

# Triggered ferroelectricity in $\text{HfO}_2$ from hybrid phonons

Seongjoo Jung, Turan Birol\*

Department of Chemical Engineering and Materials Science, University of Minnesota, Minneapolis, 55455, USA

\*Corresponding author. Email: tbirol@umn.edu

**Ferroelectric  $\text{HfO}_2$  has garnered significant attention for its promising application in high density non-volatile data storage and nanoscale transistors. However, the uncertain origin of polarization in  $\text{HfO}_2$  limits our ability to fully understand and control its ferroelectricity. The ongoing debate centers on whether  $\text{HfO}_2$  is a proper or improper ferroelectric, as it exhibits characteristics of both types. In this study, we utilize symmetry-guided first-principles quantum mechanical (DFT) calculations to accurately map the energy landscape and identify the coherent switching pathway of  $\text{HfO}_2$  by voltage. Our findings reveal two key insights. First, ferroelectricity in  $\text{HfO}_2$  is driven by a triggered mechanism through coupling between the stable polar mode and hybrid non-polar modes. Second, unusually high polarization arises from the hybrid modes, which consists solely of non-polar modes. The results fundamentally transforms the perspective on polarization in  $\text{HfO}_2$  and resolve conflicting characteristics observed, offering valuable guidance for superior technological applications.**

Since the discovery of ferroelectricity  $\text{HfO}_2$ -based thin films [1], it has been heralded as a promising candidate for future ferroelectric technologies for its compatibility with existing silicon technology, stable ferroelectricity down to sub-nanometer thicknesses [2, 3], and minimal domain-wall energy cost [4]. In addition to serving as a potential high-density memory storage medium [5], it offers lower power consumption operation in transistors [6, 7].  $\text{HfO}_2$  also exhibits distinctive electromechanical properties, apart from traditional ferroelectric materials [8, 9].

While the ferroelectric phase of  $\text{HfO}_2$  has been identified with the orthorhombic space group  $\text{Pca2}_1$  (#21), the origin of ferroelectricity in this phase remains elusive. This lack of understanding limits the ability to effectively control certain unfavorable properties, such as the high coercive field, slow domain wall propagation and formation of non-ferroelectric phases [10–13]. In general, the origin of ferroelectricity can be classified as either *proper*, where polarization results from an unstable structural mode (phonon) with polar symmetry [14], or *improper*, where it is driven by one or more unstable non-polar modes through their coupling with the polar mode [15, 16].  $\text{HfO}_2$  exhibits characteristics that both align with and challenge aspects of each mechanism.

The absence of a polar structural instability, specifically the  $\Gamma_4^-$  mode, suggests that the ferroelectricity in fluorite  $\text{HfO}_2$  ( $\text{Fm}\bar{3}\text{m}$ , #225) is improper in nature [4]. Several other factors also support this theory. No anomalies are observed in the Born effective charges [17–19], and depolarization field does not effectively suppress the polarization [2, 3, 20]. Also, out-of-plane polarization is induced when an in-plane tensile strain is applied [21], suggesting strong polar and non-polar mode interactions. However, the couplings necessary for improper ferroelectricity are forbidden in fluorite structure.

This observation led to proposal of proper ferroelectricity in  $\text{HfO}_2$ . Notably,  $\text{HfO}_2$ -based thin films are not reported to encounter the same challenges in electric switching associated with improper ferroelectrics [22], and a drastic dielectric enhancement is observed near the ferroelectric transi-

tion temperature [23]. Alternative pathways to ferroelectricity have been suggested, involving lower symmetry parent structures such as  $\text{Pmab}$  (#57) [24, 25],  $\text{Pcnb}$  (#60) [26], and  $\text{Cmme}$  (#67) [27] phases. Recently, the proper ferroelectricity of  $\text{HfO}_2$  and  $\text{ZrO}_2$  has been attributed to the softening of the transverse optical mode [28]. However, the explanations of proper ferroelectricity in  $\text{HfO}_2$  requires one or more of following assumptions, each with certain limitations: a higher energy parent structure, substantial strain, or polar phases that differ from the experimentally observed  $\text{Pca2}_1$ . Importantly, the proposed mechanisms for proper ferroelectricity do not align with the antiferroelectric-ferroelectric continuity [1, 3, 29] in fluorite systems, and result in paraelectricity when ferroelectricity is suppressed.

There are other explanations for ferroelectricity in  $\text{HfO}_2$  that do not fit into the categories of proper or improper ferroelectrics. One notable mechanism is by the negative bi-quadratic coupling between polar ( $\Gamma_4^-$ ) and non-polar mode ( $X_{5,y}^+$ ) [30], spontaneously through large tensile strain along one of the in-plane axes which is reported to induce the non-polar mode instability [31]. A trilinear coupling of modes derived from the parent phase  $\text{P4}_2/\text{nmc}$  was also identified as the origin of ferroelectricity [32]. The polar phase of  $\text{ZrO}_2$ , which shares the same symmetry, has been investigated and attributed to non-linear interactions between the  $X_5^+$  modes too, represented by a spline function [33].

While these studies offer valuable insight, there is no consensus on a model that explains the ferroelectricity in  $\text{HfO}_2$ . In this study, we employ symmetry-guided expansions of energy and polarization by Landau-Ginzburg-Devonshire (LGD) theory [34] with first-principles density functional theory (DFT), which have proven successful in modeling and elucidating the novel origins of ferroelectricity in many systems, such as multiferroic hexagonal manganites [18, 35] and Ruddlesden-Popper perovskites [16, 36]. This methodology and our results reveal two key, previously unreported findings. First, ferroelectricity in  $\text{HfO}_2$  is driven by a “hybrid-triggered” mechanism involving multiple trilinear and quad-

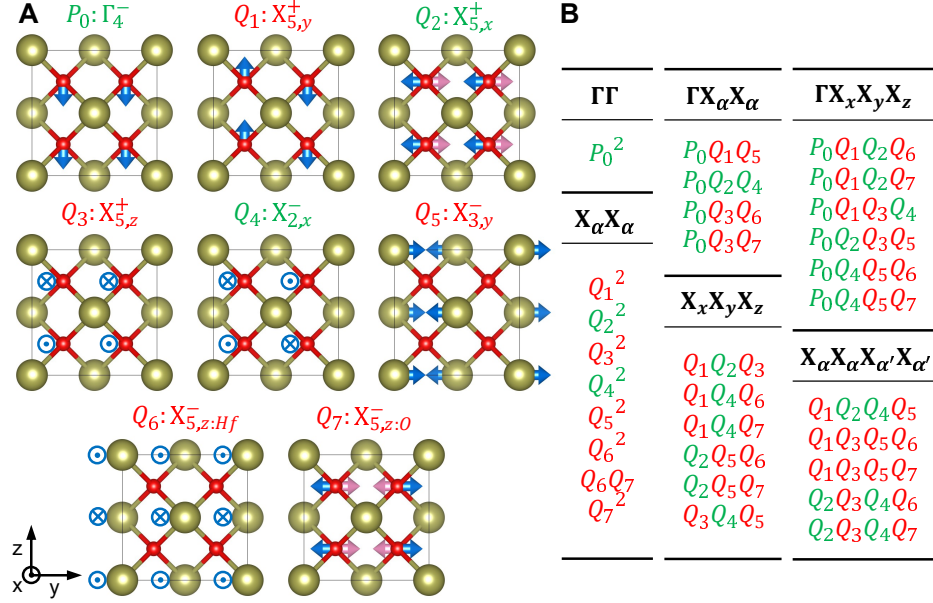


**Fig. 1: Modes and unique couplings in fluorite HfO<sub>2</sub>.** (A) Eight modes observed in the ferroelectric Pca2<sub>1</sub> phase of HfO<sub>2</sub>. Blue arrows and signs represent ionic displacements in the front half of the unit cell ( $x = 0.75$  in direct coordinates for oxygen), and the pink arrows represent those in the rear half ( $x = 0.25$ ). (B) Unique 2nd, 3rd, and 4th-order couplings among modes. Modes that can condense in the dielectric phase are highlighted in green, whereas modes that condense in the triggered phase are shown in red.

linear couplings of stable modes. Second, the hybrid zone-boundary modes, consisting of a combination of multiple symmetry-modes, exhibit exceptionally high polarization, contributing over  $\sim 50\%$  of the bulk value and offering novel properties from previously unexplored interplay between dipoles.

We begin by analyzing the crystal structure of the polar phase of HfO<sub>2</sub> (orthorhombic Pca2<sub>1</sub>) by decomposing the difference between it and the high-symmetry reference structure (fluorite Fm $\bar{3}$ m) into the symmetry-modes. There are eight relevant modes, which are labeled by the irreducible representations (irreps) of the parent space group as shown in Fig. 1 [33, 37, 38].  $P_0$  denotes the order parameter of the polar zone-center mode ( $\Gamma_4^-$ ), while the remaining parameters,  $Q_i$ , correspond to non-polar zone-boundary modes.  $Q_4$  represents the only unstable mode ( $X_{2,x}^-$ ) which has non-zero amplitude in the centrosymmetric Acaa (#68) phase. The Acaa phase is a more likely candidate for the non-polar structure of HfO<sub>2</sub> under tensile strain than the frequently assigned P4<sub>2</sub>/nmc (#137) phase according to the energies from DFT (fig. S1), consistent with the experimentally observed changes in aspect ratio and interlattice spacing [2, 3, 39].

The wavevectors of the zone-boundary modes are essential for understanding couplings between them (fig. S2). These wavevectors are not necessarily parallel to the direction of ionic displacements in real space; for instance, the ionic displacements of  $Q_1$  are along the  $z$  direction, while the wavevector points to the  $y$  direction. Unlike previous studies that label the modes by ionic displacement [4, 31, 33], we label them by their wavevectors.

Combinations of order parameter amplitudes that remain invariant under all symmetry operations of the space group (and hence transform as the  $\Gamma_1^+$  irrep) constitute the most general invariant polynomial. Fig. 1B lists the unique mode couplings that are present in this polynomial. Only terms derived from these couplings contribute to the LGD energy in its Taylor expansion around the high-symmetry phase. Consequently, the energy landscape of ferroelectric HfO<sub>2</sub> can be adequately represented using these terms up to a sufficient order, and insight about the mechanism behind ferroelectricity can be extracted from it. The second-order terms are limited to simple quadratic or bilinear terms of the same irreps. In the third order, there are only trilinear terms that can be divided into two forms:  $\Gamma X_\alpha X_\alpha$  couplings (involving one  $\Gamma$ -point mode and two X-point modes of the same wavevector) and  $X_x X_y X_z$  couplings (involving three X-point modes of different wavevectors). Similarly, quadlinear terms include  $\Gamma X_x X_y X_z$  and  $X_\alpha X_\alpha X_{\alpha'} X_{\alpha'}$  categories. While there are other fourth order terms, they do not play an important role in reducing the symmetry, and hence we do not list them.

With these insights, we now proceed to explore the origin of ferroelectricity in HfO<sub>2</sub>, where trilinear and quadlinear couplings provide a pathway for what we dub “hybrid-triggered ferroelectricity”. For simplicity, we introduce a following expression of electric enthalpy  $H$  [40, 41] using hypothetical polar (along lattice vector  $\mathbf{c}$ ) and non-polar order

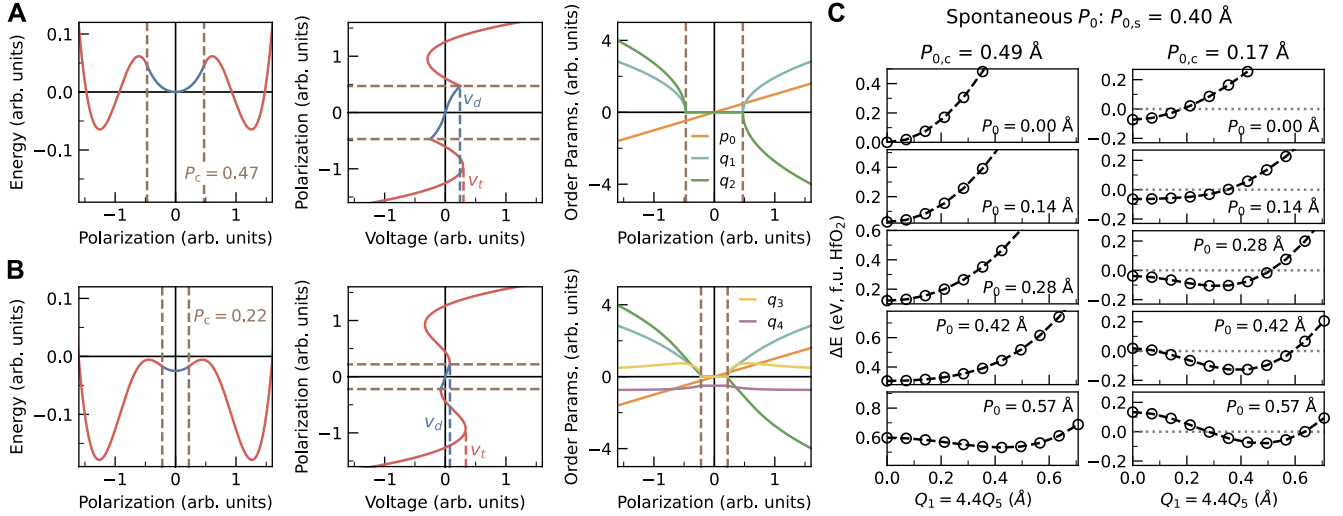


**Fig. 2: Hybrid-triggered ferroelectricity.** Energy-polarization (left), polarization-voltage (middle), and order parameters-polarization (right) relations of hybrid-triggered ferroelectrics: (A) modeled using Equation 1, and (B) incorporating an additional coupling term  $q_1q_3q_4$ . The presence of this additional coupling significantly reduces the critical polarization required to induce triggered ferroelectricity. (C) DFT-calculated energies of HfO<sub>2</sub>, illustrating hybrid-triggered ferroelectricity. The results compare scenarios where all other order parameters are fixed to zero (left) and fully relaxed (right). The critical polarization value  $P_{0,c}$  decreases from 0.49 Å to 0.17 Å.

parameters  $p_0$  and  $q_i$ :

$$H = \frac{\beta_0}{2}p_0^2 + \frac{\beta_1}{2}q_1^2 + \frac{\beta_2}{2}q_2^2 + \gamma p_0q_1q_2 + \frac{\delta_0}{4}p_0^4 + \frac{\delta_{12}}{2}q_1^2q_2^2 - v(\lambda p_0) \quad (1)$$

The variable  $v$  represents the voltage across unit cell along  $c$ , and  $\lambda$  corresponds to the mode effective charge of the polar mode normalized by lattice constant  $c$ . We consider the case where all coefficients are as positive, thus there is no soft mode that can give rise to ferroelectricity. The sign of  $\gamma$  does not matter, since it is determined by the definition of the zone boundary order parameters.

An example of solution to Equation 1 is shown in Fig. 2A. Below a critical value of the polar order parameter,  $|P_{0,c}| = \sqrt{\beta_1\beta_2}/|\gamma|$  (Supplementary Text), the system behaves as a dielectric with no contribution to energy from the trilinear coupling. This region is shown with blue lines. However, once  $|P_0|$  exceeds  $|P_{0,c}|$  by application of voltage, the hybrid mode  $q_1q_2$  becomes unstable inducing a phase transition to the polar phase where both  $q_1$  and  $q_2$  condense simultaneously (shown in red lines)—similar to the “avalanche” transition in Aurivillius compounds [42], and the predicted transitions by quadratic-linear couplings [43]. The simplest explanation to this phenomenon is that  $\gamma p_0$  acts as a tunable coefficient for second-order hybrid mode term  $q_1q_2$ . We refer to the pre-trigger phase as the dielectric phase and the post-trigger phase as the “triggered” phase.

A key distinction exists between improper and triggered ferroelectricity, though both arise from couplings between polar and non-polar modes. Improper ferroelectricity involves

unstable non-polar modes—either single or hybrid [18,36]—coupled to the polar mode. As a result, polarization switching in improper ferroelectrics requires changing the direction of a non-polar mode present in the structure, which introduces an energy barrier that does not directly couple with applied voltage (Fig. 3). Triggered ferroelectricity, by contrast, does not rely on unstable modes. It arises from couplings of hard non-polar modes with the polar mode (fig. S3). When polarization surpasses a critical threshold due to applied voltage, hybrid modes condense and the system moves to a different global minimum of energy. Unlike either proper and improper ferroelectricity, the mechanism underlying triggered ferroelectricity requires no additional instabilities.

This fundamental difference renders triggered ferroelectrics more useful for applications than improper ferroelectrics. For example, the energy barrier associated with switching of a non-polar order parameter is absent in triggered ferroelectricity. The triggered mechanism also aligns with the observed dielectric increase upon heating, akin to a first-order transition between ferroelectric and dielectric phases [43]. Notably, this is the only mechanism proposed so far that is compatible with the continuous evolution of antiferroelectricity to ferroelectricity in ZrO<sub>2</sub>-based thin films [44].  $P$ - $v$  plot of Fig. 2A shows existence of two distinct critical voltages,  $v_d$  derived from the dielectric phase, and  $v_t$  from the triggered phase. In the case where transition to the dielectric phase during polarization switching is merely transient ( $v_d < v_t$ ), it results in a ferroelectric hysteresis. Conversely, if the dielectric phase persists and manifests as a non-transient state during polarization switching ( $v_d > v_t$ ), it leads to the formation of an antiferroelectric-like double hysteresis.

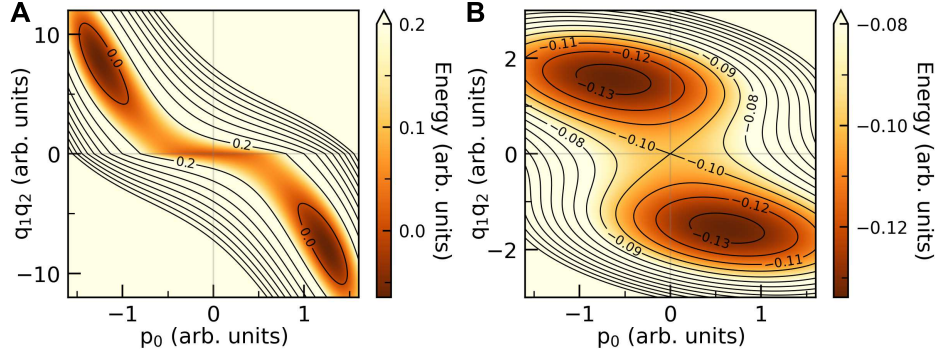


**Fig. 3: Coherent switching barrier of hybrid-triggered and hybrid-improper ferroelectrics.** Example of an energy contour diagram from LGD model of (A) Hybrid triggered ferroelectrics (Equation 1) and (B) Hybrid improper ferroelectrics. The former switch through a barrier nonparallel to  $p_0$  axis, while the latter encounter an intrinsic energy barrier parallel to the  $p_0$  axis associated with the switching of either one of the non-polar modes, which does not directly couple with voltage.

Our DFT calculations also confirm the triggered ferroelectricity in HfO<sub>2</sub>. The modes of HfO<sub>2</sub>  $P_0$ ,  $Q_1$ , and  $Q_5$  exhibit symmetries consistent with those suggested by Equation 1. We set all other displacements to zero and compute the crystal's energy as a function of the hybrid mode  $Q_1Q_5$ , maintaining a fixed ratio between  $Q_1$  and  $Q_5$ , while  $P_0$  is held at progressively increasing values. The resulting energy plots are displayed in the left panel of Fig. 2C, where the critical value for triggered ferroelectricity is  $|P_{0,c}|$  is 0.49 Å. When  $P_0$  is below this threshold, the hybrid mode increases the energy of HfO<sub>2</sub>. For  $P_0$  exceeding 0.49 Å, the energy of HfO<sub>2</sub> begins to decrease as a function of increasing hybrid mode order, revealing the hybrid mode instability.

Nevertheless, attributing the emergence of ferroelectricity a single trilinear coupling term  $P_0Q_1Q_5$  proves insufficient, as the calculated value of  $|P_{0,c}|$  is higher than the spontaneous  $P_0$  in the ferroelectric Pca2<sub>1</sub> phase,  $|P_{0,s}| = 0.40$  Å. It turns out that all the trilinear and quadlinear couplings contribute to the triggering mechanism in HfO<sub>2</sub>, except for  $P_0Q_2Q_4$ ,  $Q_1Q_3Q_5Q_6$ , and  $Q_1Q_3Q_5Q_7$ . If two trilinear or quadlinear couplings share a hybrid mode component that is inactive pre-trigger, they can condense simultaneously with reduced  $P_{0,c}$  (Supplementary Text, equation S13). This is illustrated in Fig. 2B, where the addition of trilinear term  $q_1q_3q_4$  (including soft mode  $q_4$ ) to Equation 1 reduces  $P_c$ . Similarly in HfO<sub>2</sub>, all the relevant couplings collectively induce a single transition in which all inactive modes in the dielectric phase undergo condensation at a unified and reduced critical value  $|P_{0,c}|$ . In the right panel of Fig. 2C, DFT energies are shown for the same values of  $P_0$ ,  $Q_1$ , and  $Q_5$  as the left panel, but now allowing all other order parameters to relax to a non-zero value. This adjustment reveals a substantial decrease in  $P_{0,c}$  from 0.49 Å to 0.17 Å.

Even after addressing the roles of multiple trilinear and quadlinear couplings, an important aspect of this transition remains unexplained. As demonstrated in previous studies [24, 31], when the DFT energy of HfO<sub>2</sub> is accurately plotted as a function of the polar order parameter, a cusp emerges in

the curve. This cusp does not appear in our demonstrations of hybrid-triggered ferroelectricity so far, as it is not a feature necessarily derived from the mechanism itself. A major contribution to this energy cusp is from an underappreciated factor which also connects to the origin of strong trilinear couplings in HfO<sub>2</sub>: the polarization arising from hybrid non-polar modes themselves. The hybrid modes  $Q_1Q_5$ ,  $Q_2Q_4$ ,  $Q_3Q_6$ , and  $Q_3Q_7$ , which couple with the polar mode in HfO<sub>2</sub>, break all the inversion symmetries present in the crystal and transforms exactly as the polarization itself ( $\Gamma_4^-$ ) (table S2).

The broken inversion symmetry from non-polar modes is a well-established characteristic of hybrid-improper ferroelectrics [45]. Typically, the combination of two non-polar modes leads to a nonzero amplitude of the polar structural order parameter, which is the only significant source of polarization. The case of HfO<sub>2</sub> does not fit in to this usual scenario. The polarization of HfO<sub>2</sub> from DFT in its ferroelectric Pca2<sub>1</sub> phase under 1% epitaxial tensile strain is 0.56 C/m<sup>2</sup>. The contributions from the hybrid modes  $Q_1Q_5$ ,  $Q_2Q_4$ ,  $Q_3Q_6$ , and  $Q_3Q_7$  are -0.02, -0.22, -0.05, and -0.05 C/m<sup>2</sup> respectively—the hybrid polarizations collectively account for -60% of the net polarization. Thus, the direct coupling of hybrid modes with voltage, along with local electrostatic interactions, cannot be neglected in HfO<sub>2</sub>, contrary to other improper or hybrid-improper ferroelectrics.

Accordingly, a new term representing the electronic polarization induced by the hybrid mode must be added to Eq. 1, such that  $\lambda p_0 \rightarrow \lambda p_0 + \mu q_1q_2$ . Here,  $\mu$  acts as higher order mode effective charge, and corresponds to the second derivative of polarization with respect to non-polar atomic displacements (equation S25). Such a variable is not commonly introduced before. Solution of the resulting equation with the same coefficients as Equation 1 is shown in Fig. 4A. The polarization of the hybrid mode is against the direction of the polar mode increases the value of  $P_{0,c}$ . This addition generates the cusp in the energy vs polarization plot and reveals more aspects of the phase transition. Not only are there overlapping regions of polarization in the transition pathway, but also the



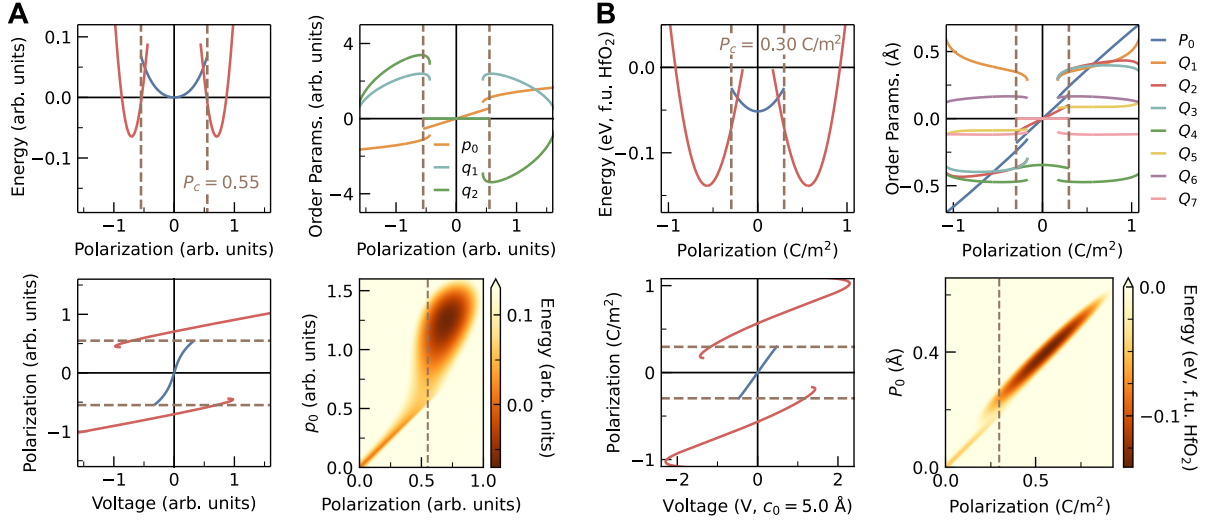


**Fig. 4: The effect of polar hybrid modes on triggered ferroelectricity.** (A) Plots for a hybrid-triggered ferroelectric material with polar hybrid mode, including energy-polarization (top left), polarization-voltage (bottom left), order parameters-polarization (top right), and two-dimensional energy- $P_0, P$  (bottom right) modeled with additional hybrid mode contribution to polarization to Equation 1. The triggered ferroelectric phase is separated from the dielectric phase in the two-dimensional energy plot, introducing an additional layer of hysteresis and a disruptive phase transition. (B) Coherent switching pathway of HfO<sub>2</sub> via the hybrid-triggered mechanism. Five order parameters that remain zero in the dielectric phase condense together at  $P_c = 0.30$  C/m<sup>2</sup> disruptively.

voltage and the order parameters in these overlapping regions are discontinuous, resulting in a disruptive phase transition where all the order parameters abruptly shift as polarization increases.

The energy plotted as a function of  $P_0$  and  $P$  provides further insight into this transition. (Fig. 4A, bottom right). When  $\mu$  is zero, the data in this plot is restricted to a one-dimensional line, as  $P$  cannot assume a value different from  $\lambda P_0$ , and vice versa. However, when  $\mu$  is non-zero,  $P$  and  $P_0$  are independent. Two distinct local minima emerge in this plot: the dielectric phase where the hybrid mode is inactive, and the triggered phase where they condense. As  $\mu$  increases, the triggered phase's local minimum separates more from the  $P = \lambda P_0$  line, eventually disconnecting entirely from the dielectric phase's local minimum. Thus, a slight increase in polarization above  $P_c$  causes a sudden jump in all order parameters, including  $P_0$ . The pathway from the triggered phase to the dielectric phase differ from the pathway from the dielectric phase to the triggered phase as the local minima are completely separated, leading to overlapping polarization regions and additional hysteresis in the switching pathway.

We apply these insights to HfO<sub>2</sub> under 1% epitaxial tensile strain to map the complete coherent ferroelectric phase transition pathway. From the coefficient obtained from the regression of DFT energies to LGD theory (fig. S4), we generate the plots in Fig. 4B. The critical polarization is 0.30 C/m<sup>2</sup>. In the dielectric phase without applied voltage, only  $Q_4$  is non-zero; upon applying voltage,  $P_0$  and  $Q_2$  condense. At 0.47 V/unit cell (u.c.), ferroelectricity is triggered, causing a simultaneous jump in five other order parameters. The voltage needed to switch polarization is higher than the triggering

voltage, reaching about 1.4 V/u.c.. The separation of two local minima is clearly visible in the two-dimensional energy landscape. Note that the proper ferroelectric switching pathway via the Pcam (#57) phase is also observed from this model, but requires higher voltage of 2.3 V/u.c., and is geometrically restricted in non-periodic boundary conditions. Thus, it is reasonable to conclude that HfO<sub>2</sub> will switch through the Acaa phase via the hybrid-triggered mechanism.

Finally, one critical question remains: what makes the hybrid modes so polar? The answer lies more in the fluorite structure itself rather than in a unique property of the Hf-O bonds. In fact, the Hf-O bond is relatively simple electronically due to the high electropositivity of Hf, compared to bonds such as Ti-O which are known to enable ferroelectricity in perovskites through hybridization [46]. Although the Hf-O bond is mostly ionic, it gains more covalent character as the Hf-O bond length decreases. This results in bond-to-bond charge transfer associated with ionic displacements in each mode. Fig. 5A shows a (010) plane of oxygens ( $y = 0.75$ ) and surrounding Hf atoms in the conventional cell. When ions displace according to  $-Q_4$  or  $Q_3$ , charge transfers towards  $+x$  between the Hf-O bonds in the upper half, and towards  $-x$  in the lower half. Fig. 5B shows this charge transfer from DFT, in the form of cuts of charge density change on Hf-O planes. The opposing direction of charge transfer between bonds results in an overall non-polar structure.

However, if ions then displace according to  $Q_2$  or  $-Q_7$  starting from the distorted structure by  $-Q_4$  or  $Q_3$ , charge is transferred upward around each oxygen ion in the crystal, as the charge transfer from the shortened bonds surpasses that from the extended bonds (Fig. 5C). This results in a sig-

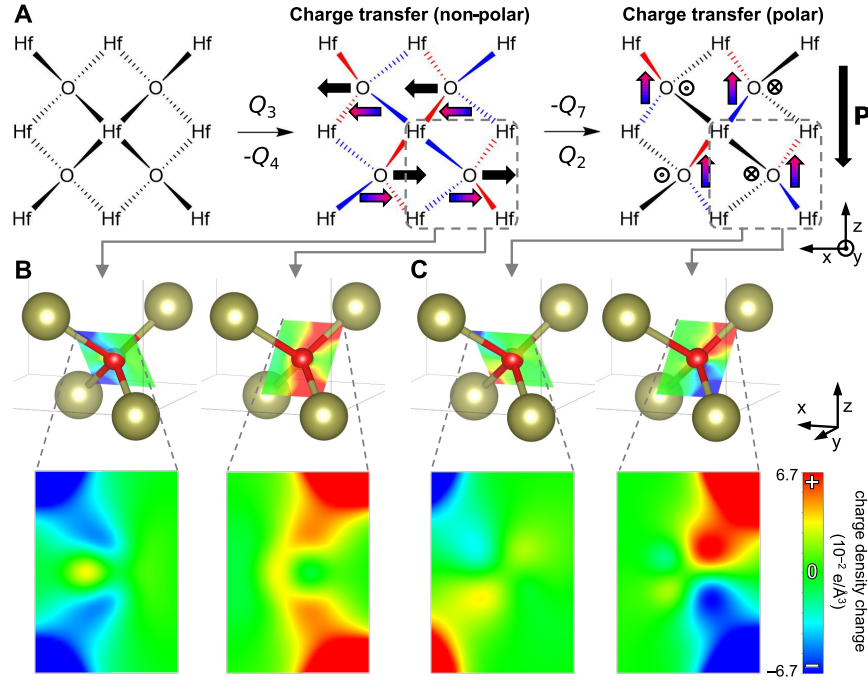


**Fig. 5: The origin of polar hybrid modes in fluorite structure.** (A) A (010) plane of oxygens ( $y = 0.75$ ) and surrounding Hf atoms in fluorite  $\text{HfO}_2$  unit cell with gradient-colored arrows indicating charge transfer from the elongated Hf-O bonds (blue) to the shortened bonds (red). (B) Charge transfer resulting from the  $-Q_4$  or  $Q_3$  mode around highlighted oxygen ion. The plane containing the two bonds directed towards  $+x$  shows charge loss (left), whereas the plane containing the two bonds directed towards  $-x$  shows charge gain. (C) Charge transfer resulting from the  $Q_2$  or  $-Q_7$  mode starting from condensed  $-Q_4$  or  $Q_3$  mode. There is minimal charge transfer between the two extended bonds in the  $+x$  direction (left), while there is significant charge transfer between the two shortened bonds in the  $-x$  direction resulting in net polar structure.

nificant downward polarization purely from electronic dipole effects, without any ionic contribution. This aligns with the observation that the Born effective charges are enhanced by only relatively small amounts in the high-symmetry phase, but they are dramatically different in different phases [19]. The nontrivial sources of polarization in this system lies not in the first derivatives with respect to displacements, but in the second derivatives. Also this purely electronic dipole, coupled with an oppositely oriented ionic dipole, can enhance the stability of ferroelectricity in ultra-thin  $\text{HfO}_2$ , as the depolarization field from one polarization source stabilizes the other, further strengthening the trilinear interaction.

Our findings fundamentally transform the traditional interpretation of polarization in oxides as a linear function of charged ions' displacements, especially in  $\text{HfO}_2$ . For example,  $\text{HfO}_2$  was thought to consist of non-polar spacer layers and polar layers, based on the displacement of oxygen ions along the  $z$  direction. Our findings show that  $\text{HfO}_2$  can exhibit substantial polarization  $P_z$  even in the absence of ionic displacements along  $z$ . The discovery of multicomponent hybrid-triggered ferroelectricity combined with the large polarization arising from hybrid modes resolve longstanding questions about the ferroelectric behavior of thin-film  $\text{HfO}_2$  and lays the foundation for superior ferroelectric applications.

## References and Notes

- [1] T. Böske, J. Müller, D. Bräuhäus, U. Schröder, U. Böttger, Ferroelectricity in hafnium oxide thin films. *Applied Physics Letters* **99** (10), 102903 (2011).
- [2] S. S. Cheema, *et al.*, Enhanced ferroelectricity in ultrathin films grown directly on silicon. *Nature* **580** (7804), 478–482 (2020).
- [3] S. S. Cheema, *et al.*, Emergent ferroelectricity in subnanometer binary oxide films on silicon. *Science* **376** (6593), 648–652 (2022).
- [4] H.-J. Lee, *et al.*, Scale-free ferroelectricity induced by flat phonon bands in  $\text{HfO}_2$ . *Science* **369** (6509), 1343–1347 (2020).

- [5] D. A. Buck, *Ferroelectrics for digital information storage and switching*, Ph.D. thesis, Massachusetts Institute of Technology, Department of Electrical Engineering (1952).
- [6] S. Salahuddin, S. Datta, Use of negative capacitance to provide voltage amplification for low power nanoscale devices. *Nano letters* **8** (2), 405–410 (2008).
- [7] M. A. Alam, M. Si, P. D. Ye, A critical review of recent progress on negative capacitance field-effect transistors. *Applied Physics Letters* **114** (9) (2019).
- [8] J. Liu, S. Liu, L. Liu, B. Hanrahan, S. Pantelides, Origin of pyroelectricity in ferroelectric HfO<sub>2</sub>. *Physical Review Applied* **12** (3), 034032 (2019).
- [9] S. Dutta, *et al.*, Piezoelectricity in hafnia. *Nature Communications* **12** (1), 7301 (2021).
- [10] D. Zhou, *et al.*, Electric field and temperature scaling of polarization reversal in silicon doped hafnium oxide ferroelectric thin films. *Acta Materialia* **99**, 240–246 (2015).
- [11] P. Buragohain, *et al.*, Nanoscopic studies of domain structure dynamics in ferroelectric La: HfO<sub>2</sub> capacitors. *Applied Physics Letters* **112** (22) (2018).
- [12] U. Schroeder, M. H. Park, T. Mikolajick, C. S. Hwang, The fundamentals and applications of ferroelectric HfO<sub>2</sub>. *Nature Reviews Materials* **7** (8), 653–669 (2022).
- [13] J. Schimpf, *et al.*, Interface effects in the phase determination of Hf<sub>0.5</sub>Zr<sub>0.5</sub>O<sub>2</sub> epitaxial thin films. *APL Materials* **13** (1) (2025).
- [14] *Modes (or symmetry-modes)* refer to the displacement patterns of ions, forming an orthonormal basis for the overall displacement of the ions in the crystal which brings the dynamical matrix to block-diagonal form with the smallest possible blocks [47].
- [15] P. Toledano, J.-C. Toledano, *Landau Theory Of Phase Transitions, The: Application To Structural, Incommensurate, Magnetic And Liquid Crystal Systems*, vol. 3 (World Scientific Publishing Company) (1987).
- [16] N. A. Benedek, M. A. Hayward, Hybrid improper ferroelectricity: a theoretical, computational, and synthetic perspective. *Annual Review of Materials Research* **52** (1), 331–355 (2022).
- [17] P. Ghosez, J.-P. Michenaud, X. Gonze, Dynamical atomic charges: The case of ABO<sub>3</sub> compounds. *Physical Review B* **58** (10), 6224 (1998).
- [18] B. B. Van Aken, T. T. Palstra, A. Filippetti, N. A. Spaldin, The origin of ferroelectricity in magnetoelectric YMnO<sub>3</sub>. *Nature materials* **3** (3), 164–170 (2004).
- [19] S. Fan, *et al.*, Vibrational fingerprints of ferroelectric HfO<sub>2</sub>. *npj Quantum Materials* **7** (1), 32 (2022).
- [20] N. Sai, C. J. Fennie, A. A. Demkov, Absence of critical thickness in an ultrathin improper ferroelectric film. *Physical review letters* **102** (10), 107601 (2009).
- [21] M. H. Park, H. J. Kim, Y. J. Kim, T. Moon, C. S. Hwang, The effects of crystallographic orientation and strain of thin Hf<sub>0.5</sub>Zr<sub>0.5</sub>O<sub>2</sub> film on its ferroelectricity. *Applied Physics Letters* **104** (7) (2014).
- [22] Y. S. Oh, X. Luo, F.-T. Huang, Y. Wang, S.-W. Cheong, Experimental demonstration of hybrid improper ferroelectricity and the presence of abundant charged walls in (Ca,Sr)<sub>3</sub>Ti<sub>2</sub>O<sub>7</sub> crystals. *Nature materials* **14** (4), 407–413 (2015).
- [23] U. Schroeder, *et al.*, Temperature-Dependent Phase Transitions in Hf<sub>x</sub>Zr<sub>1-x</sub>O<sub>2</sub> Mixed Oxides: Indications of a Proper Ferroelectric Material. *Advanced Electronic Materials* **8** (9), 2200265 (2022).
- [24] Y. Qi, S. E. Reyes-Lillo, K. M. Rabe, “Double-path” ferroelectrics and the sign of the piezoelectric response. *arXiv preprint arXiv:2204.06999* (2022).
- [25] H. Aramberri, J. Íñiguez, Theoretical approach to ferroelectricity in hafnia and related materials. *Communications Materials* **4** (1), 95 (2023).
- [26] A. Raeliarijaona, R. Cohen, Hafnia HfO<sub>2</sub> is a proper ferroelectric. *Physical Review B* **108** (9), 094109 (2023).

- [27] Y. Qi, K. M. Rabe, Competing phases of  $\text{HfO}_2$  from multiple unstable flat phonon bands of an unconventional high-symmetry phase. *arXiv preprint arXiv:2412.16792* (2024).
- [28] R. Cao, *et al.*, Softening of the optical phonon by reduced interatomic bonding strength without depolarization. *Nature* **634** (8036), 1080–1085 (2024).
- [29] J. Muller, *et al.*, Ferroelectricity in simple binary  $\text{ZrO}_2$  and  $\text{HfO}_2$ . *Nano letters* **12** (8), 4318–4323 (2012).
- [30] J. Holakovský, A new type of the ferroelectric phase transition. *Physica status solidi (b)* **56** (2), 615–619 (1973).
- [31] S. Zhou, J. Zhang, A. M. Rappe, Strain-induced antipolar phase in hafnia stabilizes robust thin-film ferroelectricity. *Science Advances* **8** (47), eadd5953 (2022).
- [32] F. Delodovici, P. Barone, S. Picozzi, Trilinear-coupling-driven ferroelectricity in  $\text{HfO}_2$ . *Physical Review Materials* **5** (6), 064405 (2021).
- [33] S. E. Reyes-Lillo, K. F. Garrity, K. M. Rabe, Antiferroelectricity in thin-film  $\text{ZrO}_2$  from first principles. *Physical Review B* **90** (14), 140103 (2014).
- [34] A. P. Levanyuk, I. Burc Misirlioglu, M. Baris Okatan, Landau, Ginzburg, Devonshire and others. *Ferroelectrics* **569** (1), 310–323 (2020).
- [35] C. J. Fennie, K. M. Rabe, Ferroelectric transition in  $\text{YMnO}_3$  from first principles. *Physical Review B—Condensed Matter and Materials Physics* **72** (10), 100103 (2005).
- [36] E. Bousquet, *et al.*, Improper ferroelectricity in perovskite oxide artificial superlattices. *Nature* **452** (7188), 732–736 (2008).
- [37] This study considers  $\text{HfO}_2$  under 1% biaxial tensile strain of and out-of-plane polarization. Although the biaxial strain imposes a tetragonal  $I4/mmm$  parent phase, we reference irreducible representations from the cubic phase for direct connection with existing literature [33]. Irreducible representations from  $I4/mmm$  parent phase and corresponding displacement patterns can be found in Table S1.
- [38] Symmetry-modes should be distinguished from *normal modes* which are derived from the eigenvectors of the dynamical matrix. While  $P_0$  and  $Q_1$  through  $Q_5$  serve as both symmetry-modes and normal modes,  $Q_6$  and  $Q_7$  solely represent symmetry-modes, not normal modes. The discussion of stable and unstable modes is generally confined to normal modes; however, these terms are somewhat flexibly applied to  $Q_6$  and  $Q_7$ , as all  $X_5^-$  normal modes are stable.
- [39] S. S. Cheema, *et al.*, Ultrathin ferroic  $\text{HfO}_2$ – $\text{ZrO}_2$  superlattice gate stack for advanced transistors. *Nature* **604** (7904), 65–71 (2022).
- [40] M. Stengel, N. A. Spaldin, D. Vanderbilt, Electric displacement as the fundamental variable in electronic-structure calculations. *Nature Physics* **5** (4), 304–308 (2009).
- [41] S. Jung, T. Birol, Octahedral Rotation Induced, Antiferroelectric-like Double Hysteresis in Strained Perovskites. *Nano Letters* (2025), doi:<https://doi.org/10.1021/acs.nanolett.4c05972>.
- [42] I. Etxebarria, J. Perez-Mato, P. Boullay, The role of trilinear couplings in the phase transitions of Aurivillius compounds. *Ferroelectrics* **401** (1), 17–23 (2010).
- [43] Y. M. Gufan, V. Torgashev, Phenomenological theory of changes in multicomponent order parameters. *Sov. Phys. Sol. St.* **22** (6), 951–956 (1980).
- [44] S. Jung, T. Birol, Hybrid-triggered antiferroelectric-ferroelectric continuity in thin film  $\text{ZrO}_2$ . *In preparation*.
- [45] A. B. Harris, Symmetry analysis for the Ruddlesden-Popper systems  $\text{Ca}_3\text{Mn}_2\text{O}_7$  and  $\text{Ca}_3\text{Ti}_2\text{O}_7$ . *Physical Review B—Condensed Matter and Materials Physics* **84** (6), 064116 (2011).
- [46] R. E. Cohen, Origin of ferroelectricity in perovskite oxides. *Nature* **358** (6382), 136–138 (1992).
- [47] H. T. Stokes, B. J. Campbell, D. M. Hatch, ISOTROPY Software Suite, <https://iso.byu.edu>.
- [48] G. Kresse, J. Furthmüller, Efficient iterative schemes for ab initio total-energy calculations using a plane-wave basis set. *Physical review B* **54** (16), 11169 (1996).



- [49] J. P. Perdew, *et al.*, Restoring the density-gradient expansion for exchange in solids and surfaces. *Physical review letters* **100** (13), 136406 (2008).
- [50] K. Momma, F. Izumi, VESTA 3 for three-dimensional visualization of crystal, volumetric and morphology data. *Journal of applied crystallography* **44** (6), 1272–1276 (2011).
- [51] R. King-Smith, D. Vanderbilt, Theory of polarization of crystalline solids. *Physical Review B* **47** (3), 1651 (1993).
- [52] M. I. Aroyo, *et al.*, Crystallography online: Bilbao crystallographic server. *Bulg. Chem. Commun* **43** (2), 183–197 (2011).
- [53] D. M. Hatch, H. T. Stokes, INVARIANTS: program for obtaining a list of invariant polynomials of the order-parameter components associated with irreducible representations of a space group. *Journal of applied crystallography* **36** (3), 951–952 (2003).
- [54] H. T. Stokes, D. M. Hatch, FINDSYM: program for identifying the space-group symmetry of a crystal. *Journal of Applied Crystallography* **38** (1), 237–238 (2005).
- [55] B. J. Campbell, H. T. Stokes, D. E. Tanner, D. M. Hatch, ISODISPLACE: a web-based tool for exploring structural distortions. *Journal of Applied Crystallography* **39** (4), 607–614 (2006).
- [56] R. Cowley, Structural phase transitions I. Landau theory. *Advances in physics* **29** (1), 1–110 (1980).
- [57] M. H. Christensen, T. Birol, B. M. Andersen, R. M. Fernandes, Theory of the charge density wave in  $\text{AV}_3\text{Sb}_5$  kagome metals. *Physical Review B* **104** (21), 214513 (2021).

## Acknowledgments

**Funding:** This work is supported by the Office of Naval Research Grant N00014-24-1-2082. The authors acknowledge the Minnesota Supercomputing Institute (MSI) at the University of Minnesota for providing part of the computational resources that contributed to this work.

**Author contributions:** S.J. conceived the idea, designed, performed the calculations and analyzed data. T.B. supervised the research. S.J. prepared the manuscript. S.J. and T.B. edited the manuscript.

**Competing interests:** There are no competing interests to declare.

**Data and materials availability:** All data are available in the main text or the supplementary materials.

## Supplementary materials

Materials and Methods  
 Supplementary Text  
 Figs. S1 to S9  
 Tables S1 to S2  
 References (48-57)

# Supplementary Materials for Triggered ferroelectricity in HfO<sub>2</sub> from hybrid phonons

Seongjoo Jung, Turan Birol\*

\*Corresponding author. Email: tbirol@umn.edu

## This PDF file includes:

Materials and Methods  
Supplementary Text  
Figs. S1 to S9  
Tables S1 to S2

## Materials and Methods

Periodic density functional theory (DFT) calculations were performed with the Vienna ab initio simulation package (VASP) 6.4.1 [48]. Spin-orbit coupling as well as spin-polarization was tested to contribute no qualitative difference to the system. A generalized gradient approximation (GGA) exchange-correlation functional PEBsol was used [49]. The projector augmented wave (PAW) method was used to describe atom cores and the plane wave basis set was expanded to a kinetic energy maximum of 520 eV for Kohn-Sham orbitals, using valence configurations  $5p^6 6s^2 5d^2$  for Hf and  $2s^2 2p^4$  for O. Tetrahedron smearing with Blöchl corrections imposed on electrons at the Fermi level. VESTA software [50] was used for building and visualizing crystal structures.

$7 \times 7 \times 7$   $\Gamma$ -centered  $\mathbf{k}$ -point mesh was used to sample the Brillouin zone of the 12-atom supercell of perovskite HfO<sub>2</sub>. Optimization of structures was converged below  $10^{-7}$  eV of electronic energy changes and 1.0 meV/Å of maximum ionic forces. Fixed-ion calculations were converged below  $10^{-6}$  eV of energy changes. Lattice parameter for cubic HfO<sub>2</sub> were 5.020 Å. Biaxial strain was simulated by fixing lattice vectors  $\mathbf{a}$ ,  $\mathbf{b}$  and allowing  $\mathbf{c}$  to relax. (The  $\eta_{zz}$  strain has same irrep as energy for a parent structure I4/mmm, appearing implicit in the Landau equation [41]). Lattice parameters under 1% tensile strain were  $a = 5.070$  Å,  $c_0 = 5.002$  Å for I4mmm phase,  $c = 5.038$  Å for Pca2<sub>1</sub> phase,  $c = 5.112$  Å for P4<sub>2</sub>/nmc phase and  $c = 5.020$  Å for Acaa phase. Polarization was calculated using the Berry phase definition from modern theory of polarization [51].  $15 \times 15 \times 15$   $\Gamma$ -centered  $\mathbf{k}$ -point mesh, and  $160 \times 160 \times 160$  fine real space mesh was used for charge density representation of the 12-atom cubic supercell.

Space group representations, mode definitions and couplings were referred from the Bilbao Crystallographic Server [52] and FINDSYM, ISODISTORT, and INVARIANTS from the ISOTROPY software suite [47,53–55]. All modes present in both the polar and non-polar minima was be considered. (The condensed modes in the triggered phase also include those in the dielectric phase.) Additionally, we assume that no additional mode condenses exclusively between the two minima, which is a valid assumption for macroscopic modeling of ferroelectricity without domain separation where no net polarization should appear in the in-plane direction without electrode screening. The following order parameter definition involving normalization factor  $\sqrt{N}$  was used, where  $N$  is the number of primitive cells in the u.c. and  $u$  is the displacement of an ion based on the lattice parameters of high-symmetry I4/mmm structure [56]:

$$|Q| = \sqrt{\frac{\sum u_{i\alpha}^2}{N}} \quad (\text{S1})$$

$i$  denotes iteration over each ion in the u.c., and  $\alpha$  over each Cartesian directions.

The equation and coefficients used for the figures are as follows:

Fig. 2A, 3A: Equation 1,

$$(\beta_0, \beta_1, \beta_2, \gamma, \delta_0, \delta_{12}, \lambda) = (0.3, 0.2, 0.1, 0.3, 1, 0.03, 1).$$

Fig. 2B: equation S13,

$$(\beta_0, \beta_1, \beta_2, \beta_3, \beta_4, \gamma_{012}, \gamma_{134}, \delta_0, \delta_{12}, \delta_{13}, \delta_4, \lambda) = (0.3, 0.2, 0.1, 0.1, -0.4, 0.3, 0.25, 1, 0.03, 0.12, 1.6, 1).$$

Fig. 3B:

$$H = \frac{\beta_0}{2} p_0^2 + \frac{\beta_1}{2} q_1^2 + \frac{\beta_2}{2} q_2^2 + \gamma p_0 q_1 q_2 + \frac{\delta_1}{4} q_1^4 + \frac{\delta_2}{4} q_2^4 + -v(\lambda p_0) \quad (\text{S2})$$

$$(\beta_0, \beta_1, \beta_2, \gamma, \delta_1, \delta_2, \lambda) = (0.05, -0.2, -0.1, 0.02, 0.1, 0.1, 1).$$

Fig. 4A: equation S25,

$(\beta_0, \beta_1, \beta_2, \gamma, \delta_0, \delta_{12}, \lambda, \mu) = (0.3, 0.2, 0.1, 0.3, 1, 0.03, 1, 0.07)$ .

fig. S3: Equation 1,  $(\beta_1, \beta_2, \delta_0, \delta_{12}, \lambda, \nu) = (0.2, 0.1, 1, 0.03, 1, 0)$ .

The full equation and coefficients used to represent entire order parameter space of HfO<sub>2</sub> in Fig. 4B,C is:

$$\begin{aligned}
H = & \beta_0 P_0^2 + \beta_1 Q_1^2 + \beta_2 Q_2^2 + \beta_3 Q_3^2 + \beta_4 Q_4^2 + \beta_5 Q_5^2 + \beta_6 Q_6^2 + \beta_7 Q_7^2 \\
& + \gamma_{015} P_0 Q_1 Q_5 + \gamma_{024} P_0 Q_2 Q_4 + \gamma_{036} P_0 Q_3 Q_6 + \gamma_{037} P_0 Q_3 Q_7 \\
& + \gamma_{123} Q_1 Q_2 Q_3 + \gamma_{146} Q_1 Q_4 Q_6 + \gamma_{147} Q_1 Q_4 Q_7 + \gamma_{256} Q_2 Q_5 Q_6 + \gamma_{257} Q_2 Q_5 Q_7 + \gamma_{345} Q_3 Q_4 Q_5 \\
& + \delta_0 P_0^4 + \delta_{01} P_0^2 Q_1^2 + \delta_{02} P_0^2 Q_2^2 + \delta_{12} Q_1^2 Q_2^2 + \delta_{03} P_0^2 Q_3^2 + \delta_{13} Q_1^2 Q_3^2 + \delta_{23} Q_2^2 Q_3^2 + \delta_{04} P_0^2 Q_4^2 + \delta_{14} Q_1^2 Q_4^2 \\
& + \delta_{24} Q_2^2 Q_4^2 + \delta_{34} Q_3^2 Q_4^2 + \delta_4 Q_4^4 + \delta_{05} P_0^2 Q_5^2 + \delta_{15} Q_1^2 Q_5^2 + \delta_{25} Q_2^2 Q_5^2 + \delta_{35} Q_3^2 Q_5^2 + \delta_{45} Q_4^2 Q_5^2 \\
& + \delta_{06} P_0^2 Q_6^2 + \delta_{16} Q_1^2 Q_6^2 + \delta_{26} Q_2^2 Q_6^2 + \delta_{36} Q_3^2 Q_6^2 + \delta_{46} Q_4^2 Q_6^2 + \delta_{56} Q_5^2 Q_6^2 \\
& + \delta_{067} P_0^2 Q_6 Q_7 + \delta_{167} Q_1^2 Q_6 Q_7 + \delta_{267} Q_2^2 Q_6 Q_7 + \delta_{367} Q_3^2 Q_6 Q_7 + \delta_{467} Q_4^2 Q_6 Q_7 + \delta_{567} Q_5^2 Q_6 Q_7 + \delta_{667} Q_6^3 Q_7 \\
& + \delta_{67} Q_6^2 Q_7^2 + \delta_{07} P_0^2 Q_7^2 + \delta_{17} Q_1^2 Q_7^2 + \delta_{27} Q_2^2 Q_7^2 + \delta_{37} Q_3^2 Q_7^2 + \delta_{47} Q_4^2 Q_7^2 + \delta_{57} Q_5^2 Q_7^2 + \delta_{677} Q_6 Q_7^3 \\
& + \delta_{0126} P_0 Q_1 Q_2 Q_6 + \delta_{0127} P_0 Q_1 Q_2 Q_7 + \delta_{0134} P_0 Q_1 Q_3 Q_4 + \delta_{0235} P_0 Q_2 Q_3 Q_5 + \delta_{0456} P_0 Q_4 Q_5 Q_6 + \delta_{0457} P_0 Q_4 Q_5 Q_7 \\
& + \delta_{1245} Q_1 Q_2 Q_4 Q_5 + \delta_{1356} Q_1 Q_3 Q_5 Q_6 + \delta_{1357} Q_1 Q_3 Q_5 Q_7 + \delta_{2346} Q_2 Q_3 Q_4 Q_6 + \delta_{2347} Q_2 Q_3 Q_4 Q_7 \\
& - \nu(\lambda P_0 + \mu_{15} Q_1 Q_5 + \mu_{24} Q_2 Q_4 + \mu_{36} Q_3 Q_6 + \mu_{37} Q_3 Q_7)
\end{aligned} \tag{S3}$$

Unlike others such as Equation 1, this equation does not include conventional factors of  $1/n$  for the coefficients of  $Q^n$  terms. Fourth order terms  $Q_1^4, Q_2^4, Q_3^4, Q_5^4, Q_6^4, Q_7^4$  which have minimal effect in the energy (fig. S8) has been excluded from the full regression up to 4th order for better convergence in the  $P$ - $P_0$  plot.

DFT data used for regression involves combinations of following order parameters. Around I4/mmm:

$P_0 = (-0.0707, 0, 0.0707)$  Å,  $Q_1 = (-0.0707, 0, 0.0707)$  Å,  $Q_2 = (-0.0717, 0, 0.0717)$  Å,  $Q_3 = (-0.0717, 0, 0.0717)$  Å,  $Q_4 = (-0.0717, 0, 0.0717)$  Å,  $Q_5 = (-0.0152, 0, 0.0152)$  Å,  $Q_6 = (-0.0254, 0, 0.0254)$  Å,  $Q_7 = (-0.0215, 0, 0.0215)$  Å. Around Pca2<sub>1</sub>:  $P_0 = (0.3299, 0.4007, 0.4714)$  Å,  $Q_1 = (0.3088, 0.3795, 0.4503)$  Å,  $Q_2 = (0.3283, 0.4001, 0.4718)$  Å,  $Q_3 = (0.3103, 0.3820, 0.4537)$  Å,  $Q_4 = (-0.5411, -0.4694, -0.3977)$  Å,  $Q_5 = (0.0708, 0.0860, 0.1013)$  Å,  $Q_6 = (0.1344, 0.1597, 0.1851)$  Å,  $Q_7 = (-0.1398, -0.1182, -0.0967)$  Å.

## Supplementary Text

### Derivation of triggered instability

$$H = \frac{\beta_0}{2} p_0^2 + \frac{\beta_1}{2} q_1^2 + \frac{\beta_2}{2} q_2^2 + \gamma p_0 q_1 q_2 + \frac{\delta_0}{4} p_0^4 + \frac{\delta_{12}}{2} q_1^2 q_2^2 - \nu(\lambda p_0) \tag{S4}$$

All the coefficients are set positive in this equation. The process of following derivations involve 3 steps. First, we identify the partial derivative of  $H$  with respect to each order parameters.

$$\frac{\partial H}{\partial p_0} = \beta_0 p_0 + \gamma q_1 q_2 + \delta_0 p_0^3 - \lambda \nu = 0 \tag{S5}$$

$$\frac{\partial H}{\partial q_1} = \beta_1 q_1 + \gamma p_0 q_2 + \delta_{12} q_1 q_2^2 = 0 \tag{S6}$$

$$\frac{\partial H}{\partial q_2} = \beta_2 q_2 + \gamma p_0 q_1 + \delta_{12} q_1^2 q_2 = 0 \tag{S7}$$

The solution of this system of equations represent the state of this material under applied voltage as a set of order parameters. We then optimize  $q_i$  according to these equations except for  $q_1$ , as it will serve as criteria of whether condensation of  $q_1$  will increase or decrease the energy of this crystal.  $p_0$  also does not need optimization as it can be any arbitrary value due to application of voltage from equation S5.

$$q_2 = -\frac{\gamma p_0 q_1}{\beta_2 + \delta_{12} q_1^2} \tag{S8}$$

We insert this expression of  $q_i$  back to equation S6

$$\begin{aligned}
\frac{\partial H}{\partial q_1} &= \beta_1 q_1 + \gamma p_0 \left( -\frac{\gamma p_0 q_1}{\beta_2 + \delta_{12} q_1^2} \right) + \delta_{12} q_1 \left( -\frac{\gamma p_0 q_1}{\beta_2 + \delta_{12} q_1^2} \right)^2 \\
&= q_1 \left( \frac{\beta_1 \delta_{12}^2 q_1^4 + 2(\beta_1 \beta_2 \delta_{12}) q_1^2 + \beta_1 \beta_2^2 - \beta_2 \gamma^2 p_0^2}{(\beta_2 + \delta_{12} q_1^2)^2} \right)
\end{aligned} \tag{S9}$$

The sign of equation S9 at infinitesimal value of  $q_1$  determines whether condensation of  $q_1$  increase or decrease  $H$ . If it is negative for an infinitesimal positive value of  $q_1$ , it will decrease  $H$  and the hybrid mode  $-q_1 q_2$  will condensate spontaneously. If it is positive, it will increase  $H$  and remain inactive. Thus if we search for a condition that renders  $(\partial H / \partial q_1) / q_1$  negative at  $q_1 = 0$ , we can find the critical condition of  $p_0$  that will trigger the hybrid mode instability.

$$\left. \frac{1}{q_1} \frac{\partial H}{\partial q_1} \right|_{q_1=0} = \frac{\beta_1 \beta_2^2 - \beta_2 \gamma^2 p_0^2}{\beta_2^2} < 0 \quad (\text{S10})$$

$$p_0^2 > \frac{\beta_1 \beta_2}{\gamma^2} \quad (\text{S11})$$

This determines the critical value of  $p_0$ ,  $p_{0,c}$ :

$$|p_{0,c}| = \frac{\sqrt{\beta_1 \beta_2}}{|\gamma|} \quad (\text{S12})$$

### Derivation of triggered instability with additional couplings

$$\begin{aligned} H = & \frac{\beta_0}{2} p_0^2 + \frac{\beta_1}{2} q_1^2 + \frac{\beta_2}{2} q_2^2 + \frac{\beta_3}{2} q_3^2 + \frac{\beta_4}{2} q_4^2 + \gamma_{012} p_0 q_1 q_2 + \gamma_{134} q_1 q_3 q_4 \\ & + \frac{\delta_0}{4} p_0^4 + \frac{\delta_4}{4} q_4^4 + \frac{\delta_{12}}{2} q_1^2 q_2^2 + \frac{\delta_{13}}{2} q_1^2 q_3^2 - v(\lambda p_0) \end{aligned} \quad (\text{S13})$$

$q_4$  corresponds to the order parameter of a soft mode, thus this equation has a special condition  $\beta_4 < 0$ . First, determine the partial derivatives.

$$\frac{\partial H}{\partial p_0} = \beta_0 p_0 + \gamma_{012} q_1 q_2 + \delta_0 p_0^3 - \lambda v = 0 \quad (\text{S14})$$

$$\frac{\partial H}{\partial q_1} = \beta_1 q_1 + \gamma_{012} p_0 q_2 + \gamma_{134} q_3 q_4 + \delta_{12} q_1 q_2^2 + \delta_{13} q_1 q_3^2 = 0 \quad (\text{S15})$$

$$\frac{\partial H}{\partial q_2} = \beta_2 q_2 + \gamma_{012} p_0 q_1 + \delta_{12} q_1^2 q_2 = 0 \quad (\text{S16})$$

$$\frac{\partial H}{\partial q_3} = \beta_3 q_3 + \gamma_{134} q_1 q_4 + \delta_{13} q_1^2 q_3 = 0 \quad (\text{S17})$$

$$\frac{\partial H}{\partial q_4} = \beta_4 q_4 + \gamma_{134} q_1 q_3 + \delta_4 q_4^3 = 0 \quad (\text{S18})$$

Second, optimize  $q_i$  ( $i \neq 1$ ).

$$q_2 = -\frac{\gamma_{012} p_0 q_1}{\beta_2 + \delta_{12} q_1^2} \quad (\text{S19})$$

$$q_3 = -\frac{\gamma_{134} q_1 q_4}{\beta_3 + \delta_{13} q_1^2} = -\frac{\gamma_{134} q_1 \sqrt{-\frac{\beta_4}{\delta_4}}}{\beta_3 + \delta_{13} q_1^2} \quad (\text{S20})$$

$$|q_4| = \sqrt{-\frac{\beta_4}{\delta_4}} \quad (\text{S21})$$

Note that  $q_4$  can be optimized for pre-trigger dielectric phase, as we are searching for  $p_{0,c}$ . Third, insert  $q_i$  back to  $(\partial H / \partial q_1) / q_1$  and determine the condition it is negative at  $q_1 = 0$ .

$$\left. \frac{1}{q_1} \frac{\partial H}{\partial q_1} \right|_{q_1=0} = \frac{\beta_1 \beta_2^2 \beta_3^2 - \beta_2 \beta_3^2 \gamma_{012}^2 p_0^2 - \beta_2^2 \beta_3 \gamma_{134}^2 q_4^2}{\beta_2^2 \beta_3^2} < 0 \quad (\text{S22})$$

$$p_0^2 > \frac{\beta_1 \beta_2 \beta_3 - \beta_2 \gamma_{134}^2 q_4^2}{\beta_3 \gamma_{012}^2} = \frac{\beta_1 \beta_2 - \frac{\beta_2 (-\beta_4) \gamma_{134}^2}{\beta_3 \delta_4}}{\gamma_{012}^2} \quad (\text{S23})$$

$$|p_{0,c}| = \frac{\sqrt{\beta_1 \beta_2 - \frac{\beta_2 (-\beta_4) \gamma_{134}^2}{\beta_3 \delta_4}}}{|\gamma_{012}|} \quad (\text{S24})$$



The numerator is reduced from  $\sqrt{\beta_1\beta_2}$  to  $\sqrt{\beta_1\beta_2 - \frac{\beta_2(-\beta_4)\gamma_{134}^2}{\beta_3\delta_4}}$ , so multiple coupling reduces the value of shared trigger. From equation S19 and S20, simultaneous condensation of  $q_1$ ,  $q_2$  and  $q_3$  is shown.

What we show is that with the additional trilinear coupling, instead of an additional trigger being created leading to second phase transition, the critical value  $p_{0,c}$  is decreased substantially and shared among both couplings—the simultaneous condensation of  $q_1$ ,  $q_2$ , and  $q_3$  occurs. In other words, the hybrid mode  $q_1q_2q_3$  instability occurs at a lower  $p_0$  compared to just  $q_1q_2$  or  $q_1q_3$ .

### Derivation of triggered instability with polar hybrid mode

$$H = \frac{\beta_0}{2}p_0^2 + \frac{\beta_1}{2}q_1^2 + \frac{\beta_2}{2}q_2^2 + \gamma p_0q_1q_2 + \frac{\delta_0}{4}p_0^4 + \frac{\delta_{12}}{2}q_1^2q_2^2 - v(\lambda p_0 + \mu q_1q_2) \quad (S25)$$

First, determine the partial derivatives.

$$\frac{\partial H}{\partial p_0} = \beta_0p_0 + \gamma q_1q_2 + \delta_0p_0^3 - \lambda v = 0 \quad (S26)$$

$$\frac{\partial H}{\partial q_1} = \beta_1q_1 + \gamma p_0q_2 + \delta_{12}q_1q_2^2 - \mu v q_2 = 0 \quad (S27)$$

$$\frac{\partial H}{\partial q_2} = \beta_2q_2 + \gamma p_0q_1 + \delta_{12}q_1^2q_2 - \mu v q_1 = 0 \quad (S28)$$

Second, optimize  $q_i$  ( $i \neq 1$ ).

$$q_2 = -\frac{(\gamma p_0 - \mu v)q_1}{\beta_2 + \delta_{12}q_1^2} \quad (S29)$$

Here,  $v$  also has to be represented as a function of  $p_0$  and the coefficients. From equation S26:

$$v = \frac{\beta_0p_0 + \delta_0p_0^3}{\lambda} \quad (S30)$$

$$q_2 = -\frac{[(\gamma - \frac{\mu\beta_0}{\lambda})p_0 - \frac{\mu\delta_0}{\lambda}p_0^3]q_1}{\beta_2 + \delta_{12}q_1^2} \quad (S31)$$

Note that  $v$  was optimized for pre-trigger dielectric phase. Third, insert  $q_i$  back to  $(\partial H/\partial q_1)/q_1$  and determine the condition it is negative at  $q_1 = 0$ . The solution is equivalent to the derivation of Equation 1, where  $\gamma p_0$  is substituted to  $\gamma p_0 - \mu v$ .

$$\frac{1}{q_1} \frac{\partial H}{\partial q_1} \Big|_{q_1=0} = \frac{\beta_1\beta_2^2 - \beta_2(\gamma p_0 - \mu v)^2}{\beta_2^2} < 0 \quad (S32)$$

$$\left( \left( \gamma - \frac{\mu\beta_0}{\lambda} \right) p_0 - \frac{\mu\delta_0}{\lambda} p_0^3 \right)^2 = \beta_1\beta_2 \quad (S33)$$

While the general solution cannot be expressed, when  $\delta_0 \sim 0$ :

$$|p_{0,c}| = \frac{\sqrt{\beta_1\beta_2}}{\left| \gamma - \frac{\mu\beta_0}{\lambda} \right|} \quad (S34)$$

Depending on the sign of  $\mu$ , the polar hybrid mode can either increase or decrease  $|p_{0,c}|$ . In the case of HfO<sub>2</sub>, the direction of polarization from second order hybrid modes always oppose the direction of polarization from the polar mode. This would correspond to the same sign of  $\gamma$  and  $\mu$ , which increases  $|p_{0,c}|$ .

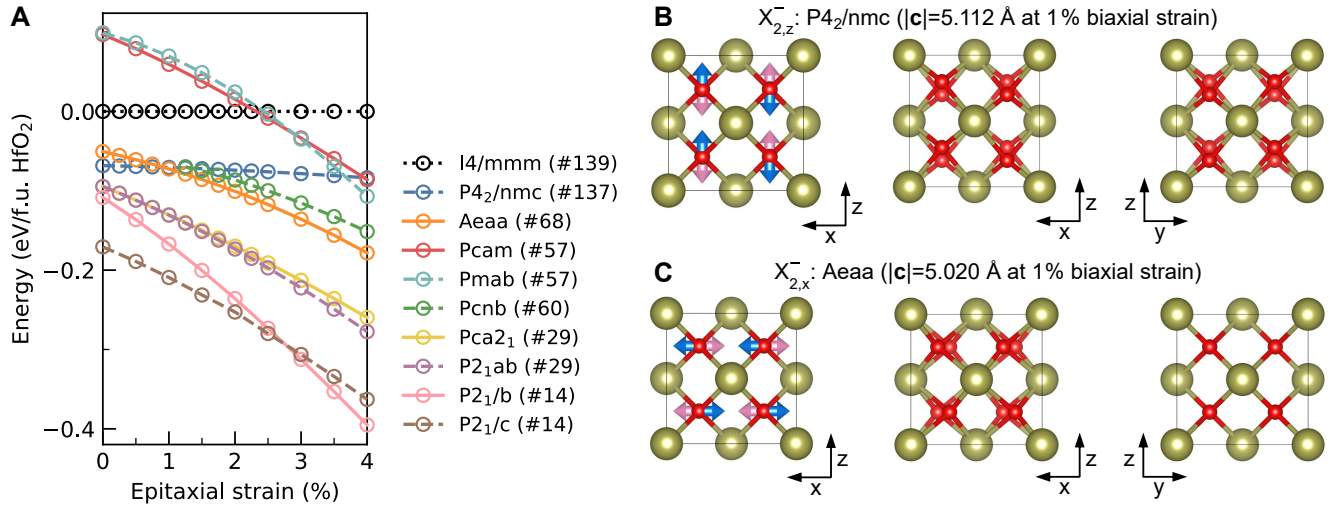


**Fig. S1: Biaxial strain phase diagram of HfO<sub>2</sub>.** (A) Solid lines indicate phases derived from  $X_{2,x}^-$ , while dashed lines represent phases derived from  $X_{2,z}^-$ . (B) Structural representation of  $X_{2,z}^-$  mode and (C)  $X_{2,x}^-$  mode. Blue arrows represent oxygen displacements in the front half of the unit cell ( $y = 0.75$  in direct coordinates), and the pink arrows represent those in the rear half ( $y = 0.25$ ). In the absence of a monoclinic lattice transformation (as well as domain-separated structures such as Pbca from [4]), the Acaa phase emerges as the most stable non-polar ground state under moderate tensile strain, derived from structural instability in the fluorite HfO<sub>2</sub>. Experimental observations of the lattice constants from [2, 3, 39] further support this. Transition from Pca2<sub>1</sub> to P4<sub>2</sub>/nmc increases the aspect ratio  $2c/(a + b)$ , whereas transition from Pca2<sub>1</sub> to Acaa reduces it. ( $c = 5.038$  Å for Pca2<sub>1</sub> phase)

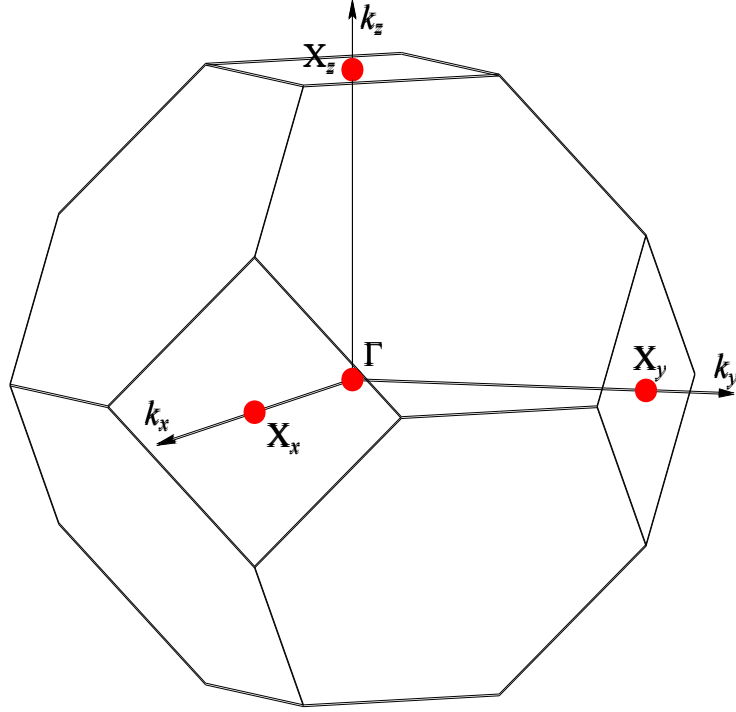


**Fig. S2: First Brillouin zone of a face-centered cubic lattice system [52].** The coordinates of the wavevectors  $k_{X_x}$ ,  $k_{X_y}$ , and  $k_{X_z}$  corresponding to the positions of the  $X_x$ ,  $X_y$ , and  $X_z$  points in reciprocal space, are  $(2\pi/a, 0, 0)$ ,  $(0, 2\pi/a, 0)$ , and  $(0, 0, 2\pi/a)$  respectively in  $(k_x, k_y, k_z)$ . The sum  $k_{X_x} + k_{X_y} + k_{X_z}$  forms a  $\Gamma$ -point modulo in reciprocal space, enabling a trilinear coupling with irrep equal to that of the energy ( $\Gamma_1^+$ ). Note that the sum of wavevectors being equal to a  $\Gamma$ -point modulo is a necessary condition for irrep equivalence with the energy, and not a sufficient one. For instance, the wavevector sum arising from the bilinear coupling  $Q_1 Q_5 (k_{X_x} + k_{X_x})$  also forms a  $\Gamma$ -point modulo but exhibits irrep equivalent to polarization ( $\Gamma_4^-$ ). Consequently, the bilinear coupling does not directly appear in the energy expression.

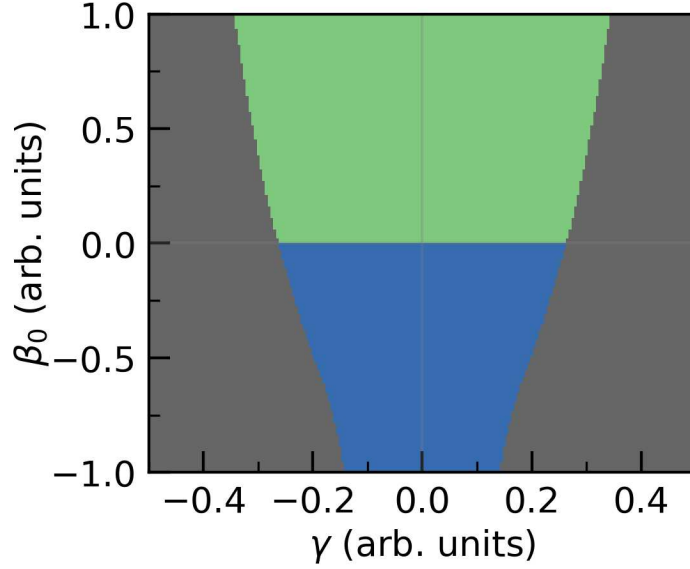


**Fig. S3: Phase diagram of a hybrid-triggered ferroelectric by Equation 1, by second-order  $p_0$  coefficient  $\beta_0$  and trilinear coupling coefficient  $\gamma$ .** Green area represent the non-polar ground state where  $p_0 = q_1 = q_2 = 0$ , blue area the proper ferroelectric ground state where  $p_0 \neq 0, q_1 = q_2 = 0$ , and the gray area the hybrid-triggered polar ground state where  $p_0, q_1, q_2 \neq 0$ . The hybrid-triggered ground state exists for cases when the polar mode is both soft and hard, if the trilinear coupling is strong enough. Similar phase diagram can be found for a hypothetical case of quadratic-linear order parameter coupling [43], and charge density wave order in kagome metals involving a trilinear coupling [57]. The tricritical points are along  $\beta_0 = 0$  for all phase diagrams. In the cases where the components of hybrid mode remain hard when  $\beta_0 = 0$ , there is a tricritical point for each sign of non-zero value of  $\gamma$ . In the case of kagome metals where all three components of trilinear coupling have the same second-order coefficient, the two tricritical points merge into one point at  $\gamma = 0$ .

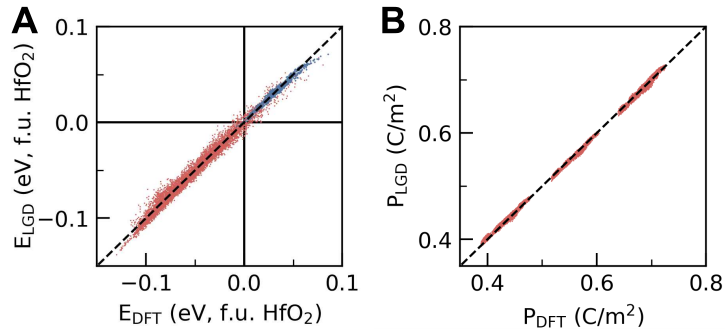


**Fig. S4: Symmetry-adapted regression of DFT data using LGD theory (A) Energy and (B) polarization data of  $\text{HfO}_2$  under 1% tensile biaxial strain.** Blue points correspond to  $3^8$  data points around the high-symmetry  $I4/mmm$  phase, while red points correspond to  $3^8$  data points around the ferroelectric  $Pca2_1$  phase.



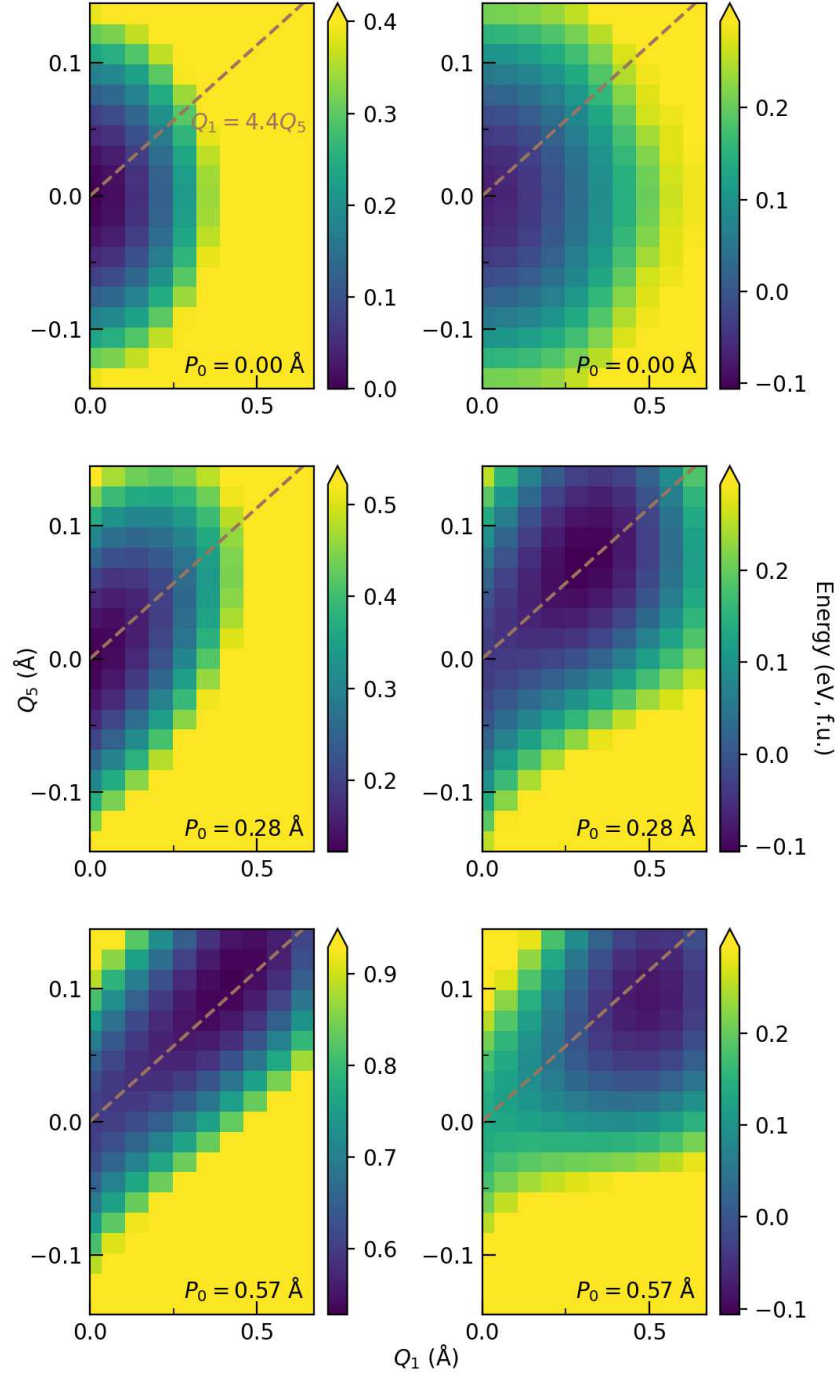


**Fig. S5: Two-dimensional DFT-calculated energies of  $\text{HfO}_2$ , illustrating hybrid-triggered ferroelectricity and  $P_0Q_1Q_5$  coupling.** The results compare scenarios where all other order parameters are fixed to zero (left) and fully relaxed (right). One-dimensional data shown in Fig. 2C is along  $Q_1 = 4.4Q_5$  line which preserve the ratio at the ferroelectric minimum. The fixed ratio is not necessarily imposed from the hybrid-triggered ferroelectricity. Note that even when the hybrid mode  $Q_1Q_5$  instability appears, individual modes  $Q_1$  and  $Q_5$  can remain hard.

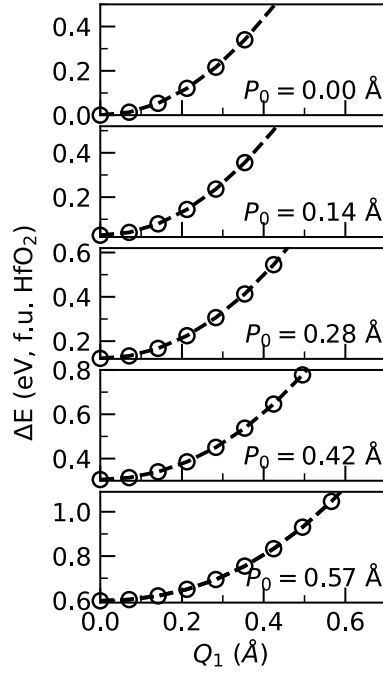


**Fig. S6: Biquadratic coupling between  $P_0$  and  $Q_1$ .** A slight negative biquadratic coupling exists between  $P_0$  and  $Q_1$  [31]. However, in contrast to the trilinear and quadlinear couplings shown in Fig. 2, this coupling between the two hard modes does not induce a new local minimum or phase transition. The negative biquadratic coupling also occurs for  $Q_1^2 Q_4^2$ ,  $Q_3^2 Q_4^2$ ,  $P_0^2 Q_5^2$ ,  $Q_3^2 Q_5^2$ ,  $Q_1^2 Q_6^2$ ,  $Q_1^2 Q_7^2$ , and  $Q_4^2 Q_7^2$  without major contribution to energy.

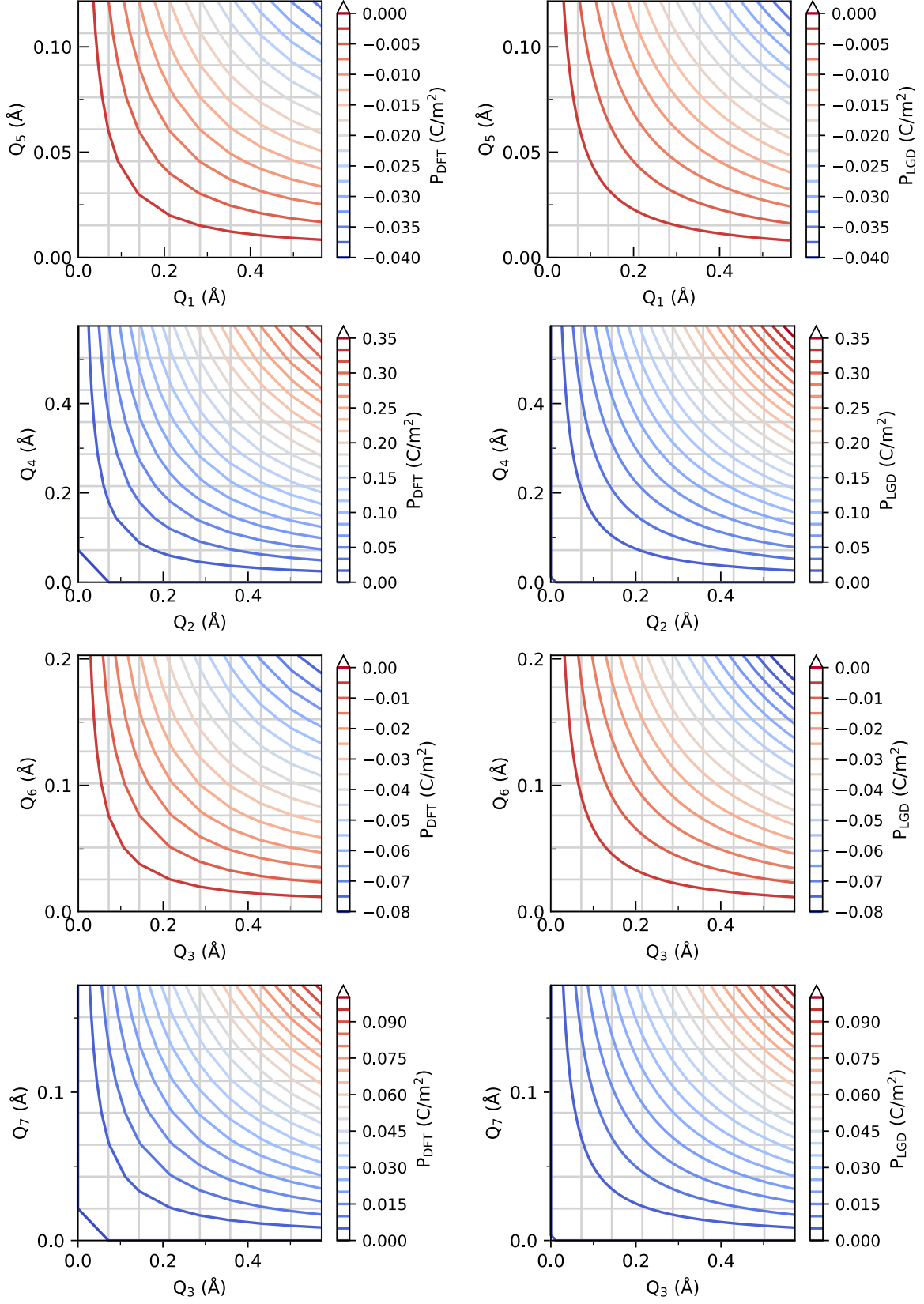


**Fig. S7: Polarization from hybrid non-polar modes.** Polarization of 1% biaxial strained  $\text{HfO}_2$  from DFT calculations (left) and symmetry-guided LGD theory up to second order (right).

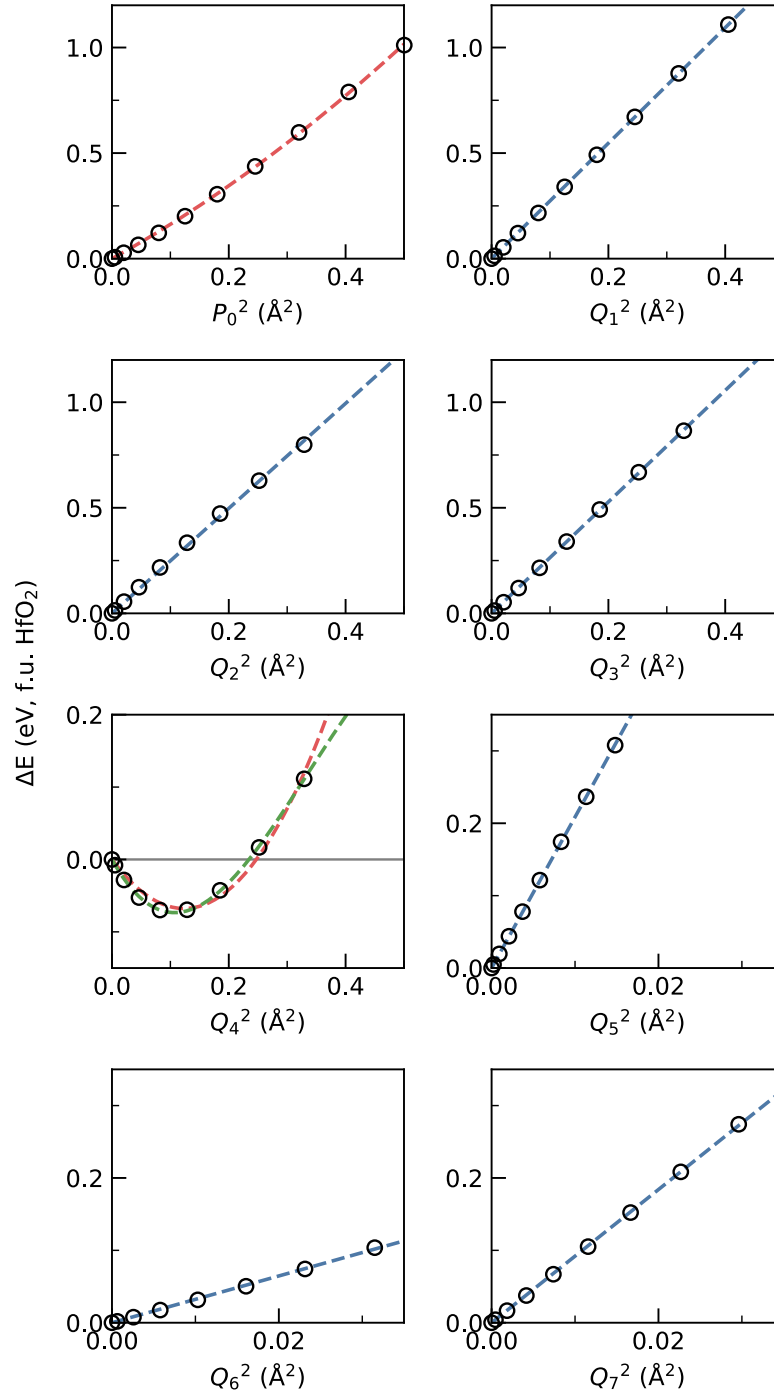


**Fig. S8: One-dimensional contribution of each modes to energy.** Blue, red and green dotted lines each represent 1st, 2nd and 3rd order regression of energy with respect to  $Q^2$  through the origin. Linear regression fits most order parameters squared, except  $P_0$  and  $Q_4$ .



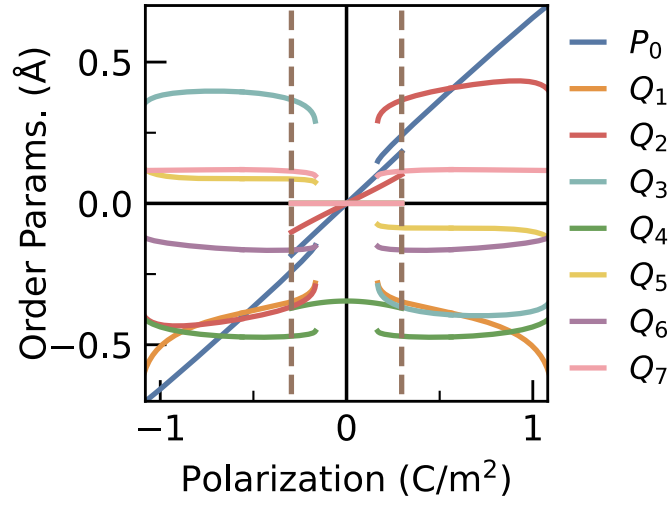


**Fig. S9: Alternative domain switching of HfO<sub>2</sub>.** Despite the presence of 8 modes, each triggered phase only have 2 domains that share the same sign of  $Q_4$ . The domains not shown in Fig. 4B is displayed here. There is equal chance of the modes condensing to each domain when the ferroelectricity is triggered.

**Table S1: Irreducible representation (irrep) of order parameters from different parent structures.** Hf ion at (0, 0, 0) and O ion at (0.25, 0.25, 0.25) in direct coordinates from high-symmetry structure is used as reference for in-phase Hf and O. Lattice transformation from  $\text{Fm}\bar{3}\text{m}$  to  $\text{I4}/\text{mmm}$  requires rotation of Cartesian bases around  $z$  axis by  $\pi/4$ , thus  $x'$  and  $y'$  directions in  $\text{I4}/\text{mmm}$  reciprocal space are different from  $\text{Fm}\bar{3}\text{m}$  reciprocal space.

Order Parameter	Irrep		Ionic displacements				Space Group
	$\text{Fm}\bar{3}\text{m}$	$\text{I4}/\text{mmm}$	$\text{Hf}_{\text{in}}$	$\text{Hf}_{\text{out}}$	$\text{O}_{\text{in}}$	$\text{O}_{\text{out}}$	
$\eta_{zz}$	$\Gamma_1^+ \oplus \Gamma_3^+$	$\Gamma_1^+$	-	-	-	-	$\text{I4}/\text{mmm}$ (#139)
$P_0$	$\Gamma_4^-$	$\Gamma_3^-$	-	-	$-u_z$	-	$\text{I4}/\text{mm}$ (#107)
$Q_1$	$X_{5,y}^+$	$X_{3,y'}^+$	-	-	$u_z$	$-u_z$	$\text{Bm}\bar{3}\text{b}$ (#64)
$Q_2$	$X_{5,x}^+$	$X_{2,x'}^+$	-	-	$u_y$	$-u_y$	$\text{Ae}\bar{a}\text{m}$ (#64)
$Q_3$	$X_{5,z}^+$	$M_5^+$	-	-	$u_x$	$-u_x$	$\text{Cc}\bar{m}\text{e}$ (#64)
$Q_4$	$X_{2,x}^-$	$X_{1,x'}^-$	-	-	$u_x$	$-u_x$	$\text{Ae}\bar{a}\text{a}$ (#68)
$Q_5$	$X_{3,y}^-$	$X_{4,y'}^-$	$u_y$	$-u_y$	-	-	$\text{Bm}\bar{3}\text{m}$ (#67)
$Q_6$	$X_{5,z}^-$	$M_5^-$	$u_x$	$-u_x$	-	-	$\text{Cc}\bar{m}\text{m}$ (#63)
$Q_7$	$X_{5,z}^-$	$M_5^-$	-	-	$u_y$	$-u_y$	$\text{Cc}\bar{m}\text{m}$ (#63)

**Table S2: Inversion breaking of the symmetry-modes.**  $i_1$  to  $i_4$  denote the inversion centers present in the high-symmetry conventional fluorite unit cell. For every inversion center  $(x, y, z)$ , there are 7 more translation induced inversion centers at  $(x+0.5, y, z)$ ,  $(x, y+0.5, z)$ ,  $(x, y, z+0.5)$ ,  $(x, y+0.5, z+0.5)$ ,  $(x+0.5, y, z+0.5)$ ,  $(x+0.5, y+0.5, z)$ , and  $(x+0.5, y+0.5, z+0.5)$ . Symbol  $\bigcirc$  indicates that the inversion center is preserved upon the condensation of the mode, while  $\times$  signifies that the inversion center is destroyed.

Inversion center	Direct coordinates			$\eta_{zz}$	$P_0$	$Q_1$	$Q_2$	$Q_3$	$Q_4$	$Q_5$	$Q_6$	$Q_7$
	$x$	$y$	$z$									
$i_1$	0	0	0	$\bigcirc$	$\times$	$\bigcirc$	$\bigcirc$	$\bigcirc$	$\times$	$\times$	$\times$	$\times$
$i_2$	0	0.25	0.25	$\bigcirc$	$\times$	$\times$	$\bigcirc$	$\times$	$\times$	$\bigcirc$	$\bigcirc$	$\bigcirc$
$i_3$	0.25	0	0.25	$\bigcirc$	$\times$	$\bigcirc$	$\times$	$\times$	$\bigcirc$	$\times$	$\bigcirc$	$\bigcirc$
$i_4$	0.25	0.25	0	$\bigcirc$	$\times$	$\times$	$\times$	$\bigcirc$	$\bigcirc$	$\bigcirc$	$\times$	$\times$